Manuscript version: Author's Accepted Manuscript

The version presented in WRAP is the author's accepted manuscript and may differ from the published version or Version of Record.

Persistent WRAP URL:

http://wrap.warwick.ac.uk/114219

How to cite:

Please refer to published version for the most recent bibliographic citation information.
If a published version is known of, the repository item page linked to above, will contain details on accessing it.

Copyright and reuse:

The Warwick Research Archive Portal (WRAP) makes this work by researchers of the University of Warwick available open access under the following conditions.

Publisher's statement:

Please refer to the repository item page, publisher's statement section, for further information.

For more information, please contact the WRAP Team at: wrap@warwick.ac.uk.

Author's Accepted Manuscript

Rational Design and Synthesis of Molecular-Sieving, Photocatalytic, Hollow Fiber Membranes for Advanced Water Treatment Applications

David K. Wang, Muthia Elma, Julius Motuzas, Wen-Che Hou, Fengwei Xie, Xiwang Zhang

Cite this article as: David K. Wang, Muthia Elma, Julius Motuzas, Wen-Che Hou, Fengwei Xie and Xiwang Zhang, Rational Design and Synthesis of Molecular-Sieving, Photocatalytic, Hollow Fiber Membranes for Advanced Water Treatment Applications, *Journal of Membrane Science* http://dx.doi.org/10.1016/j.memsci.2016.10.052

Rational Design and Synthesis of Molecular-Sieving, Photocatalytic, Hollow Fiber Membranes for Advanced Water Treatment Applications

David K. Wang[1*], Muthia Elma[1,2], Julius Motuzas[1], Wen-Che Hou[3], Fengwei Xie[4], Xiwang Zhang[5]

[1]FIM[2]Lab - Functional Interfacial Materials and Membranes Laboratory, School of Chemical Engineering, The University of Queensland, Brisbane, Queensland 4072, Australia

[2]Chemical Engineering Department, Lambung Mangkurat University, Jl. A. Yani KM 36 Banjarbaru, South Kalimantan, 70714 Indonesia.

[3]Department of Environmental Engineering, National Cheng Kung University, Tainan City 70101, Taiwan.

[4]School of Chemical Engineering, The University of Queensland, Brisbane, Queensland 4072, Australia.

[5]Department of Chemical Engineering, Faculty of Engineering, Monash University, Clayton, Victoria 3800, Australia

[*]Corresponding author: Tel: +61 7 3365 6970; Fax: +61 7 3365 4199. d.wang1@uq.edu.au

Abstract

Photocatalytic, hollow fiber membranes based on nanocomposites of titania nanoparticles and carbonaceous char were simultaneously fabricated in a single calcination step, and then optimized for the photo-degradation of pollutants and water recovery in an integrated membrane operation in this study. The physicochemical, mechanical and photocatalytic properties along with separation performance of two series of membranes were finely-tuned by systematically changing the calcination temperature (series 1: 500 – 1000 °C for 8 h holding time) and calcination time (series 2: 2 – 8 h at 600 °C). The calcined membranes were extensively characterized for morphology, thermal stability, microstructure, modulus and chemical compositions. Both constituents of titania and char are essential in deriving the desirable hollow fiber properties and membrane performance for photocatalysis and water recovery. By controlling the calcination conditions, membranes prepared at 600 °C for the 3 and 6 h duration displayed an optimal balance between enhanced mechanical strength (34 MPa) and high photo-degradation of acid orange 7 (90.4%). Membrane performance demonstrated water fluxes of 6.9 (H_2O/dark), 12.9 (H_2O/UV) 4.8 (AO7/dark) and 7.9 L m^{-2} h^{-1} (AO7/UV) with excellent organic dye rejection. Both membranes exhibited photo-induced super-hydrophilicity and defouling potential under the influence of UV light due to the photo-activation of exposed TiO_2 nanoparticles on the membrane surface. The detailed mechanism of property correlation and separation performance for the photocatalytic hollow fibers is proposed and elucidated. This work offers an innovative material for the research avenue of photocatalytic, hollow fiber membrane reactors for advanced membrane treatment applications.

Graphical Abstract

Hollow fiber membranes with molecular sieving and photocatalytic capabilities exhibited super-hydrophilicity and defouling potential under UV photo-oxidation.

1

1. Introduction

In the last 50 years, membrane research and development have gained a significant interest for separation applications and technology. The major advantages of membrane technology, particularly hollow fibers, are smaller footprint, ease of maintenance, and high separation efficiency [1], which are very appealing for industrial membrane applications. Furthermore, the class of inorganic membranes provides excellent mechanical, chemical and thermal stability, and durability over the conventional polymeric membranes [2]. Nevertheless, despite the prolific use of membrane filtration to remove harmful organic pollutants in wastewater effluents in general, its performance and lifespan are undermined by two major issues, namely (1) the increasing presence of non-biodegradable, persistent chemical contaminants in the discharged effluents and (2) the severity of membrane fouling due to a rapid build-up of the pollutants and the omnipresent bacteria on the membrane surface [3-5].

Among the various effective ways of addressing these significant problems, such as biological treatment intervention, adsorption, physical and chemical cleanings, as well as process intensification, the applications of advanced oxidation processes (AOPs) are making remarkable research grounds. The general mechanism of AOPs relies on the oxidative nature of reactive radical species generated from heterogeneous catalysts (TiO_2, ZnO, Fe_3O_4, ZnS), oxidants (e.g. ozone, H_2O_2) and/or irradiation [6-8]. Specifically, titanium dioxide (TiO_2) nanoparticles are widely investigated for its excellent photocatalytic activity, stability and anti-bacterial property [3, 9, 10]. When exposed to UV, electrons-hole pairs are generated on the surface of the nanoparticles reacting with the oxygen and water molecules to create radicals. However, the main technical barrier that impedes their commercialization is associated with the photocatalytic efficiency and post-recovery of the TiO_2 nanoparticles from the treated effluents. In order to overcome this barrier, the development of novel technologies, such as integrated ultrafiltration/microfiltration membranes, which were successfully reported for the removal of organic pollutants from water [11, 12]. However, considerations on the catalyst leaching, membrane fouling, pore blocking of TiO_2 fine powder, and the added process complexity are significant cost burdens on the operation and maintenance. Other examples of technologies are magnetic separation, catalyst immobilization, and photocatalytic TiO_2 membranes, has been recently discussed in several comprehensive thematic reviews [3, 10, 13, 14].

The use of photocatalysts and radiation together to treat and destroy highly toxic molecules, while somewhat novel in the membrane research, has been central to advanced oxidation process field. Only in the last ten years are researchers beginning to consider how these two fields may be integrated to achieve a highly-compact, multifunctional, single-unit operation [3]. The first inorganic photocatalytic TiO_2 membranes was reported on flat-sheet supported alumina substrates. Choi *et al.* demonstrated mesoporous TiO_2 films and membranes with a TiO_2 active layer on alumina support affording good adsorption and UV photocatalysis of methylene blue, whilst producing high water permeability and antifouling property [15, 16]. Since then, there has been a continued growth of interest in designing photocatalytic TiO_2 membranes as described in these recent reviews [3, 17, 18]. Despite the development to date has predominantly been

focused on flat-sheet supported membranes and catalyst-deposited membranes, the research of photocatalytic TiO_2 hollow fibers is rapidly emerging.

Earlier work involving inorganic-based hollow fibres containing TiO_2 as an additive, include ceramic [19], carbon [20-22], and hybrid [23-26] materials have demonstrated unique properties in niche membrane applications for high-temperature gas processing and water treatment. Typically, the syntheses of inorganic hollow fibers require the use of a polymer binder to hold the inorganic nanoparticles together to firstly form the green body via a spinning and phase-inversion process. This is followed by the removal of the binder at high temperatures above 1000 °C over several hours to ultimately produce the pure inorganic hollow fibers. Also, this intensive thermal treatment is essential to sinter the inorganic oxide nanoparticles together in order to achieve high mechanical strength. However, the major disadvantages of high-temperature thermal processing of TiO_2 are nucleation and grain growth leading to irreversible phase transformation [27, 28], which can significantly alter the photocatalytic properties and performance of the membranes. Therefore, it is a research challenge to control the morphology and properties of the consolidated TiO_2 matrix, and at the same time, to meet the design criteria of the compact, multifunctional hollow fibers as membrane reactors.

In this study, two series of composite hollow fibers and photocatalytic membrane reactors based on titania and binder-derived char were optimized for physicochemical-mechanical-photocatalytic-performance relationship to achieve efficient photocatalysis and purified water recovery. This was carried out by systematically varying the calcination conditions based on temperature (500 – 1000 °C; 8 h) and time (2 – 8 h; 600 °C) with comprehensive characterizations and membrane evaluations.

2. Experimental

2.1 Chemicals and materials

In this study, all the chemicals and reagents were from Sigma Aldrich (ACS grade) and used without further purification. The specific details of the Degussa P25 titanium dioxide (TiO_2) nanoparticles were reported in an earlier study [29].

2.2 Hollow Fibre Synthesis

To prepare the hollow fibers, a spinning-pyrolysis technique was employed [30]. Briefly, Degussa P25 TiO_2 powder was mixed with poly(ether imide) (PEI) and solvent (1-methyl-2-pyrrolidinone (NMP)) in a 18:25:75 ratio (w/w) for 24 h until homogenous and then degassed by vacuum for another 24 h. The spinning dope was then extruded through a tube-in-orifice spinneret (OD = 2.5 mm and ID = 0.8 mm). The pressure in the spinning dope and airgap was maintained at 4 bars and 50 mm, respectively. Phase inversion was induced from the inner side of the hollow fiber followed by the outside in deionized (DI) water bath, where the green fiber was left immersed for 24 h. Then, the TiO_2/PEI green fiber was dried for 24 h at 60 °C. Before pyrolysis, the green fiber was

3

placed inside a double open-ended quartz tube (length = 20 cm; OD = 8 mm) to minimize the geometric curvature, and then heated at a temperature in the range of 500 – 1000 °C (series 1) for a fixed 8 h holding time, or 600 °C for 2 – 8 h (series 2) using a muffle furnace without the introduction of any specialized gases. PEI was gradually pyrolysed into char with partial decomposition during the thermal process to afford the final composite, char-TiO_2 hollow fibers.

2.3 Characterization techniques

The morphological structure of the pyrolysed composite hollow fibers was examined using a field-emission scanning electron microscope (FESEM JEOL 7001F operating at 10 kV) and high-resolution transmission electron microscopy (HR-TEM) was performed on a JEOL2100 microscope equipped with energy-dispersive x-ray spectroscopy (EDS). The outer surface of the hollow fibers was examined by X-ray photoelectron Spectroscopy using a Kratos Axis ULTRA XPS incorporating an incident monochromatic radiation Al K_α X-rays (1486.6 eV) at 225 W (15 kV, 15 mA). Nitrogen sorption measurement of the hollow fibers was performed using Micromeritic TriStar 3000 instrument after degassing the samples at 200 °C overnight under vacuum on a VacPrep061. The specific surface area was determined from Brunauer, Emmett and Teller (BET) method and total pore volume was taken from the last point of the adsorption isotherm (ca. 0.94 P/P_o). The cumulative pore volume distribution was determined from adsorption branch of the isotherms using the Density Functional Theory (DFT) model of cylindrical pores with oxide surfaces. Dubinin-Astakhov and Barrett-Joyner-Halenda methods were taken to determine the average pore diameter of microporous and mesoporous materials, respectively. The char residue content of the pyrolysed hollow fibers was determined by thermal gravimetric analyzer (TGA, Mettler Toledo TGA/DSC 1 Star^e System) from room temperature to 1000 °C at a heating rate 5 °C min^{-1} and 80 mL min^{-1} flow rate of air. A three-point-bending test was performed using Instron 5543 universal machine with a set strain rate of 1 mm min^{-1} to measure the mechanical strength of the composite hollow fibers. The maximum bending strength was calculated by using the following expression for a simple tube [31],

$$\sigma = \frac{8FLD}{\pi(D^4 - d^4)}$$

where, σ is the bending strength (MPa), F is the load applied (N), and L, D and d are the span, outer diameter and the inner diameter (mm) of the hollow fiber, respectively.

The crystal structure and phase composition of the hollow fibers (after grinding) were analyzed by a powder X-ray diffraction system (XRD, Bruker AXS D8 advance, Cu-Ka radiation). By using the diffraction peak intensities of the anatase (101) and rutile (110) phases, the weight fraction of the rutile can be calculated from the following equation [32],

4

$$R_S = \frac{1}{1 + 0.8\dfrac{I_a}{I_r}}$$

where R_S is the weight fraction of the rutile phase, I_a is the diffraction peak intensity of the anatase (101) plane, I_r is the diffraction peak intensity of the rutile (110) plane [33].

2.4 Photocatalysis evaluation of the hollow fibers

The photocatalytic activity of the composite hollow fibers was evaluated using four UV-A lamps (SYLVANIA Blacklite F8W/BL350, 330 – 370 nm emission; 8 Watt each) as the UV source. Acid Orange 7 (AO7) was used as a model colour dye due to its excellent stability under UV irradiation [34]. 25 ml of AO7 (20 ppm; pH 6.5) in a quartz reactor vessel was placed concentrically at 15 cm away from the UV lamps in the UV chamber to minimize the heating effect of the UV lamps. The sintered hollow fiber membranes weighing about 50 mg (membrane surface area: approximately 1.5×10^{-4} m^2) were immersed in the AO7 solution in the reactor. 30 min dark sorption experiment was performed prior to switching on the UV lamps. The measured intensity of the UV via an intensity meter (Model 308, OAI) received on the membrane is approximately 0.17 mW cm^{-2} in the presence of AO7 solution. During the photocatalysis under UV exposure, the temperature of the reactor gradually increased from room temperature (22 °C under air condition) to about 40 ± 1 °C, of which the impact on the photo-degradation of the AO7 dye is considered insignificant based on our observations and the literature [30, 35-37]. Hence, the temperature effect is neglected in this study. The UV-Vis spectrum of the feed solution was recorded from 220 – 620 nm by a UV-Vis spectrophotometer (Evolution 220, Thermo Scientific). The concentration of AO7 was determined by measuring the absorbance at 485 nm based on an established calibration standard curve. The photocatalytic activity of the membrane can be determined by the percent degradation of AO7 in the feed solution based on the equation, AO7 degradation (%) = $(C_0 – C_t)/C_0 \times 100\%$, where C_0 and C_t are the AO7 concentration in the reactor solution before photocatalysis (after dark sorption) and at reaction time t, respectively.

2.5 Membrane performance

The permeability of the membrane was evaluated by measuring the water flux of DI water and AO7 solution with UV in a dead end permeation mode adapted for hollow fibers [38, 39]. A control experiment without UV irradiation was also conducted. As shown in Fig. 1, one end of the hollow fiber is sealed with epoxy resin and the other end is connected to a vacuum line and the permeate stream was collected in a cold trap which was immersed in a liquid nitrogen dewar. A vacuum of 1.5 kPa is applied across the membrane as the driving force. The water flux, F (L m^{-2} h^{-1}), was determined based on the equation F = $m/(A \cdot \Delta t)$, where m is the mass of permeate (L) retained in the cold trap, A is the surface-active area (m^2) of the membrane and Δt is the time measurement (h). The AO7 rejection, R (%), was calculated as R = $(C_f – C_p)/C_f \times 100\%$, where C_f and C_p are the feed and permeate concentrations of AO7. After 1 h of permeation, UV-vis spectrum of the feed and permeate was recorded.
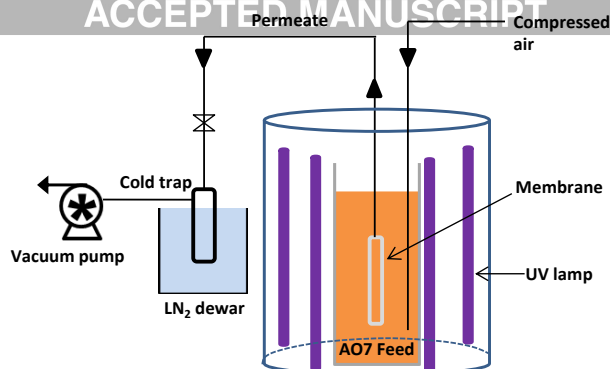
Figure 1. A customised membrane permeation and photocatalysis set-up.

3. Results

3.2 Hollow Fiber Morphology and Properties

Prior to calcination, the green hollow fiber was examined by SEM technique. Fig. 2 shows the representative SEM images of the cross-section and surface of green fiber. In general, the entire green fiber is measured in the order of approximately 2 ± 0.2 mm with a wall thickness of 500 ± 50 µm, both of which are directly dependent on a complex set of spinning parameters such as die dimension, air gaps, and dope flow rate (pressure). Moreover, the fiber morphology can be described as a typical asymmetric structure with a relatively non-porous surface, which is an important precursor for obtaining good mechanical strength and separation characteristics.
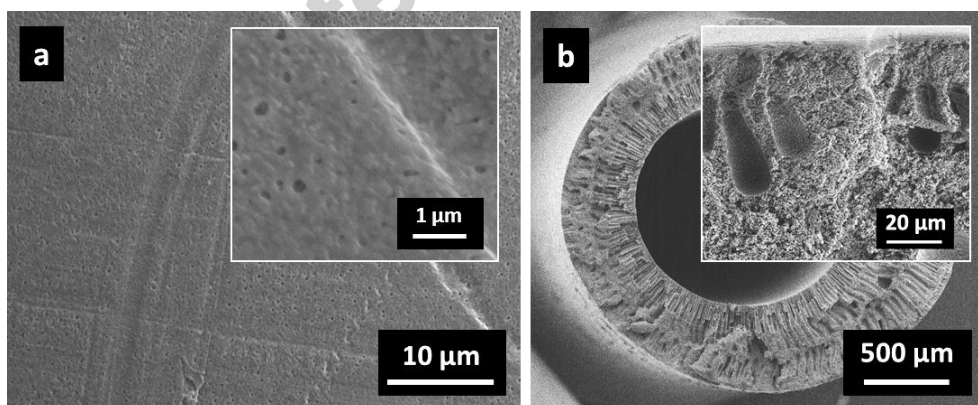

Figure 2. SEM images of green fiber (uncalcined) of the (a) outer surface and (b) cross-section with higher magnification in the inset images.

6

In Fig 2(a), the morphology of the green fiber appears to be relatively smooth with homogeneous spread of several surface defects. On closer inspection as seen in the inset, the surface is granular and nodular, which is attributed to the morphology of the TiO_2 nanoparticles. Further examination of the cross-section image in Fig. 2(b) shows that the fiber consists of large finger-like macrovoid villi extending from both the inner wall to the outer wall. Additionally, as shown by the inset, adjacent to the macrovoids are mainly composed of sponge-like microvoids, which makes up the bulk of the fiber. These specific characteristics of the fiber morphology have been well-ascribed to the thermodynamic instability of the chemical potential during the phase-inversion process [30, 40-42].

Upon calcination, two series of hollow fibers were synthesized by systematically changing the temperature from 500 to 1000 °C for a fixed holding time of 8 h (temperature-series), and the time from 3 to 8 h for a fixed temperature of 600 °C (time-series). Fig. 3 displays the SEM cross-section images of the calcined hollow fibers at the outer skin layer. Clearly, the calcination conditions strongly influence the morphology and porosity of this layer, which is an important membrane feature that dictates selectivity. From the temperature-series images (bottom row), the calcined hollow fibers are all porous with varying pore sizes and TiO_2 nanoparticle sizes, both of which increases with increasing temperature. In comparison, the time-series images of the 600 °C fibers show a less pronounced differences with a relatively dense skin layer, except for the 600-8h sample. This strongly suggests that when the fiber is calcined below a certain temperature (< 600 °C) and time (< 6 h), there is an incomplete removal of the PEI-derived phase, which forms the interstitial carbonaceous matrix between the TiO_2 nanoparticles.

To better understand the morphology of the hollow fibers, high-resolution TEM analysis was carried out. Fig. 4 displays HR-TEM images of the time-series fiber samples with the 800 °C sample for comparison. The figures clearly demonstrate that the dense inorganic TiO_2 nanoparticles are embedded within a carbonaceous matrix with some electron translucency. In fact, a close examination of this matrix on a thin section reveals a certain degree of ultra-microporosity, which is particularly evident in the 3 and 6 h images. By increasing both calcination time and temperature as seen in both of the 8 h samples, the amount of this matrix decreases and almost cannot be visually appreciated in the 800 °C image. This observation is in good agreement with the morphological analyses by the SEM images in Fig. 3.
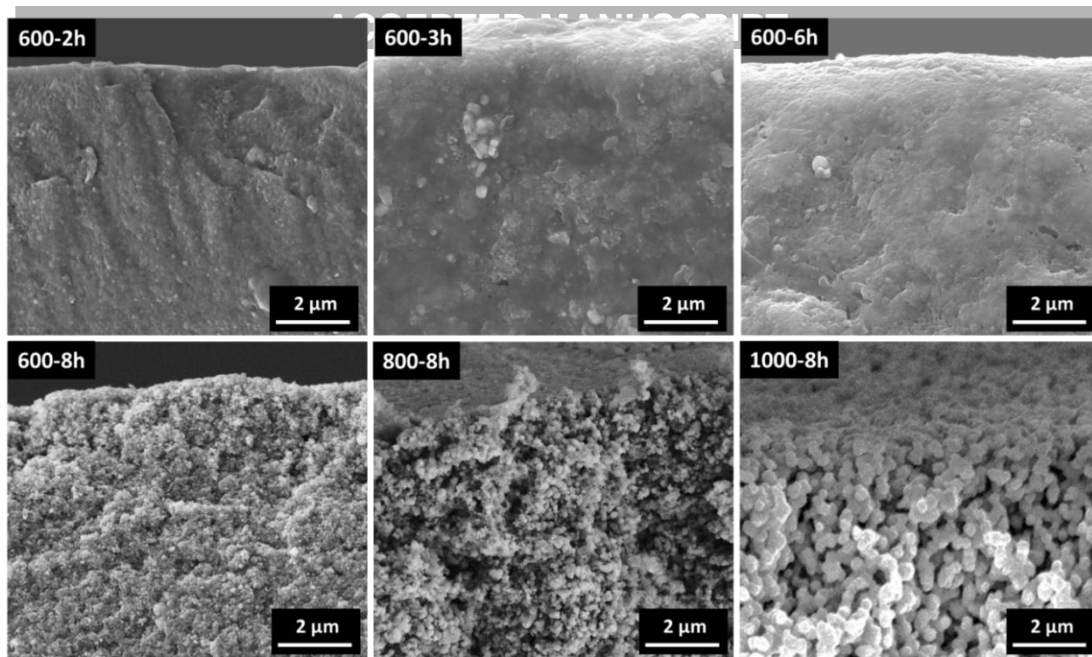
Figure 3. SEM images of the cross-section of the calcined hollow fibers as a function of calcination conditions.
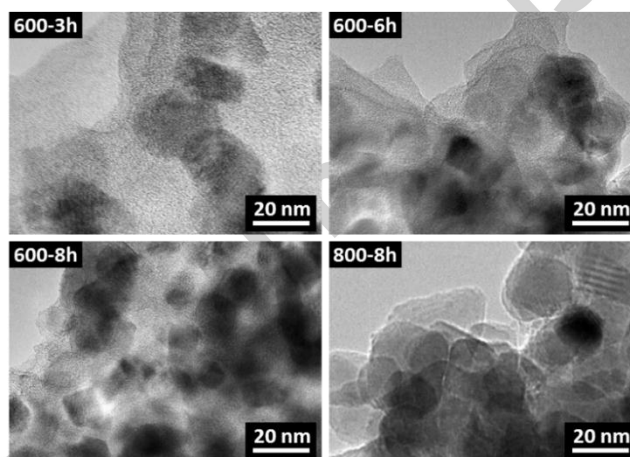

Figure 4. HR-TEM images of the calcined hollow fibers as a function of pyrolysis conditions.

Further evidence of this carbonaceous matrix was examined by thermogravimetric analysis technique. The calcine hollow fibers were heated from room temperature to 1000 °C to quantitatively determine the amount of the residual PEI-derived matrix remained within each of the hollow fibers. It is anticipated that the change in fiber mass is only attributed to the mass loss associated with the oxidative combustion of the carbonaceous matrix and not due to the TiO_2 nanoparticles. Fig. 5(a) shows the weight profile of the calcined hollow fibers for the time-series group along with the data for the 800 °C fiber, and the corresponding normalized mass loss is plotted in Fig. 5(b) for both series. From Fig. 5(a), there is a 2 to 4% weight reduction prior to

200 °C, which is due to the loss of the physi-sorbed water inside the calcined fibers. Apart from the 800 °C weight profile, the majority of the weight change occurs between 400 and 600 °C, after which the change in weight is observed to be negligible up to 1000 °C. Obviously, the mass loss of samples decreases with increasing calcination time for the 600 °C fibers. This trend is clearly depicted in Fig. 5(b). Firstly, for the temperature-series hollow fibers, it shows that the largest mass loss of 51% occurred in the 500 °C fiber followed by 8 and 3% for the 600 and 700 °C fibers, respectively. Above 700 °C calcination conditions, the mass loss is entirely due to the loss of water as there would be no carbonaceous residue remained inside the fibers under these high-temperature calcination conditions. In a similar trend, the relative amount of the carbonaceous matrix decreases with increasing calcination time for the 600 °C fibers. Interestingly, the largest difference is seen between the 6 and 8 h fibers, which further corroborates with the previous electron microscopy results.
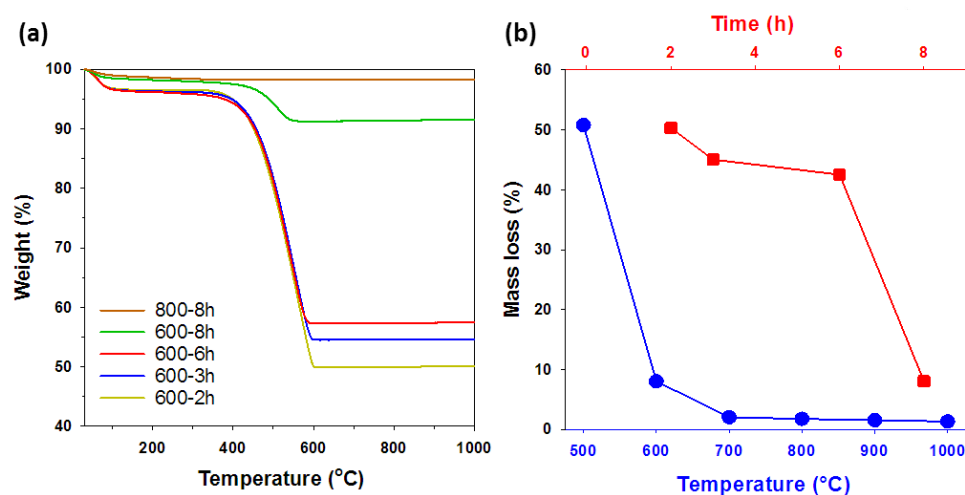

Figure 5. (a) TGA curve and (b) mass loss of the calcined hollow fibers as a function of calcination temperature (blue symbols) and time (red symbols).

The textural property of the calcined hollow fibers was further examined by N_2 physisorption technique. Fig. 6(a) and Table 1 show the N_2 physisorption isotherms and textural results (BET surface area, total pore volume and average pore diameter) of the fibers as a function of calcination temperature and time. Fig. 6(b) shows the plots of surface area and relative micropore percentage determined from the pore size distributions. Firstly in Fig. 6(a), the isotherm profiles of calcined hollow fibers in the temperature-series group reveal three types of pore regime in the system. At the 600 °C, the fiber contains all the characteristics of a microporous, mesoporous and macroporous solid. The initial rapid rise of nitrogen adsorption under the 0.2 P/P₀ partial pressure is characteristics of a microporous texture, while towards the higher partial pressures, the adsorption branch continue to increase gradually with a final large uptake of adsorption followed by a small degree of hysteresis in the desorption branch. The latter signifies capillary condensation associated with meso- and macro-porous structure. This is also evident from the loss of both the

9

surface area and microporous proportion (Fig 6(b)). For higher temperature treatment (> 700 °C), the PEI binder is completely removed leaving only the TiO$_2$ phase that causes the fiber to become a macroporous solid with a minor degree of mesoporosity as the intra- and inter-particle voids are exposed [30]. This structure is also supported by the fiber morphology as observed in the SEM images (Fig. 3). Interestingly at the other temperature extreme, the 500 °C fiber produced a negligible surface area. It is postulated that this fiber was perhaps relatively dense due to the incomplete treatment of the PEI binder, and thus, it was non-porous.
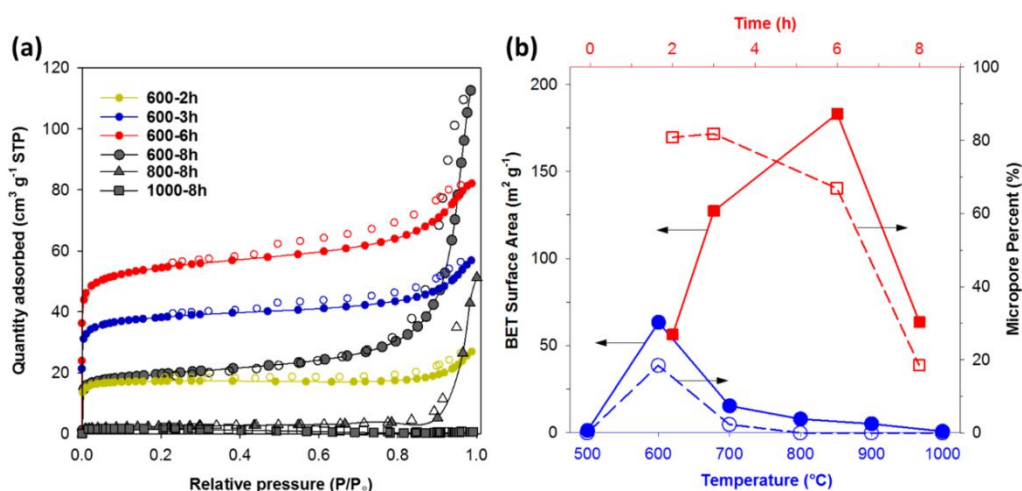

Figure 6. (a) Nitrogen adsorption (solid symbols-line) and desorption (open symbols) isotherm curves, and (b) BET surface area (full line) and micropore percent (broken line) of the calcined hollow fibers as a function of calcination temperature (blue symbols) and time (red symbols).

Table 1. Surface properties of TiO$_2$ carbon composite hollow fiber membranes with different calcination conditions.

Temp (°C)	Time (h)	BET surface area ($m^2 g^{-1}$)	Total pore volume ($cm^3 g^{-1}$)	Average pore diameter (nm)
500	8	1.2	0.001	-
600		63.3	0.161	2.82
700		15.3	0.094	28.9
800		7.8	0.041	32.9

900		5	-	-
1000		0.7	-	-
600	2	56.2	0.039	1.56
	3	127.2	0.085	1.76
	6	183.0	0.130	1.82
	8	63.3	0.161	2.82

In the time-series group, there is both characteristics of microporous and mesoporous structure in the matrix. By extending the calcination time, the degree of N_2 adsorption increases significantly, but at the same time, proportion of the mesoporous domain also builds up. This behaviour in the textural property is clearly depicted in Fig. 6(b), whereby the increase in surface area is seen from 2 to 6 h, but is marked by a decline in microporous proportion. However, by further extending the calcination time, the degree of microporosity significantly decreases as can be seen by the 70% reduction of the adsorption branch in the 8 h sample. This is attribute to the loss of the carbonaceous matrix as evidenced from the TGA results (Fig. 5(b)), leading to the revelation of a predominantly meso/macroporous solid. Such transition is demonstrated by a decline in both the surface area and micropore percentage (Fig. 6(b)).

Therefore, based on the correlation between the trends of porosity, and the TGA and SEM results, the carbonaceous matrix is of microporous, amorphous origin. By retaining a high amount of carbon matrix, the isotherm of the composite hollow fibers shows a rapid onset of N_2 adsorption at low relative partial pressure of 0.2 P/P_o. This is indicative of a highly microporous material [43]. On the other hand, by removing the carbon matrix, the TiO_2 hollow fibers fabricated by high-temperature calcination conditions (700 to 1000 °C) produced a meso/macroporous texture, which is typically described for TiO_2 nanomaterials and membranes [29, 30, 44].

The mechanical property of the hollow fiber in terms of fracture toughness was also examined by 3-point bending test. Fig. 7 displays the mechanical bending stress (MBS) of the calcined fibers with respect to temperature and time. As shown in Fig. 7, when either the temperature or time increases, MBS values of the hollow fibers decrease significantly from 95.5 (500 °C) to 3 (900 °C) MPa, and from 52 (2 h) to 13 (8 h) MPa. By systematically removing the carbon matrix, the MBS can also be seen to decline in parallel. Similarly, there is a MBS minimum region between 600 and 900 °C when only the TiO_2 phase is present. This strongly suggests that the presence of the carbon matrix improved the mechanical strength of the composite hollow fibers. However, it is noteworthy that the TiO_2 hollow fiber calcined at 1000 °C showed a rise in the mechanical strength, which is attributed to the sintering effect of the nanoparticles as confirmed by the SEM image in Fig. 3. It is well-known that inorganic hollow fibres containing alumina, titania and

11

perovskites have been routinely calcined at high-temperatures in excess of 1000 °C leading to a densified membrane matrix with improved mechanical strength [19, 45-49]. Also, it was demonstrated by Zhang *et al.*[30] that the TiO_2 hollow fibers calcined at 800 °C can only achieve a maximum bending strength of 3 MPa, which significantly improved by 10-fold at a much higher calcination temperature of 1400 °C.
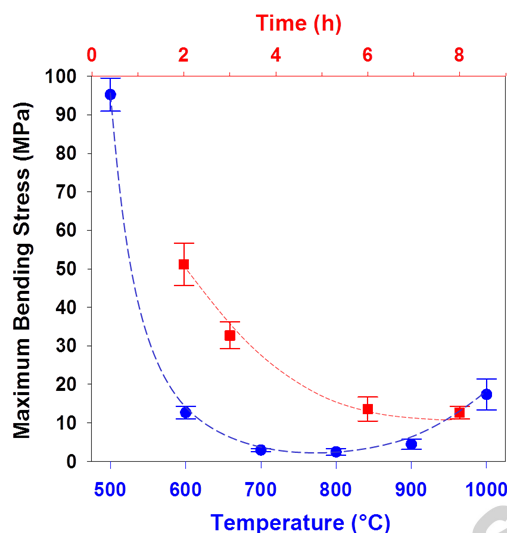

Figure 7. Maximum bending stress of the pyrolyzed hollow fibers with respect to calcination temperature (blue symbols) and time (red symbols). Dotted lines are shown to guide the eyes.

To determine the TiO_2 phase composition of the hollow fibers after calcination, the hollow fibers were grounded into powder and analysed by XRD. Fig. 8(a) and 8(b) show the XRD pattern of the fibers over the 20 – 80° 2θ region, and the corresponding weight fraction of the anatase phase determined the diffraction peak intensities of the anatase (101) and rutile (110) phases according to the equation described in the methodology. The data for Degussa P25 TiO_2 is also included for comparison. In Fig. 8(a), it can be observed that the major TiO_2 phase is anatase in all the time-series fibers, but the major peak attributes to rutile phase at 27.4° 2θ becomes more intense and pronounced with increasing calcination time. As shown in Fig. 8(b), the anatase weight fraction slowly decreases from approximately 80.1 to 67.1%. However, this is still very comparable to that of the Degussa P25 TiO_2 (81.9%). The transformation of anatase to rutile is well-known to proceed via a nucleation and growth process which is favoured at high temperatures because the rutile crystalline phase is thermodynamically more stable [50-52]. The trend of the XRD results suggests that the presence of carbon matrix surrounding the TiO_2 nanoparticles is inhibiting the extent of thermally-induced aggregation, and thus preventing the morphological transformation of the TiO_2 phases [43]. On other hand in an another study, Kordouli *et al*.[53] reported that P25 TiO_2 nanoparticles calcined at 600 °C in air loses more than 50% of the anatase fraction in the first 3 h of heat treatment. Moreover, by increasing the calcination temperature from 600 to 1000 °C, the transformation of anatase to rutile takes place and reached near completion at 800 °C and

12

thereafter [30, 53]. This is not surprising as the rutile phase is more thermodynamically stable than the anatase phase and will form by thermally-induced aggregation of the anatase TiO$_2$ [36].
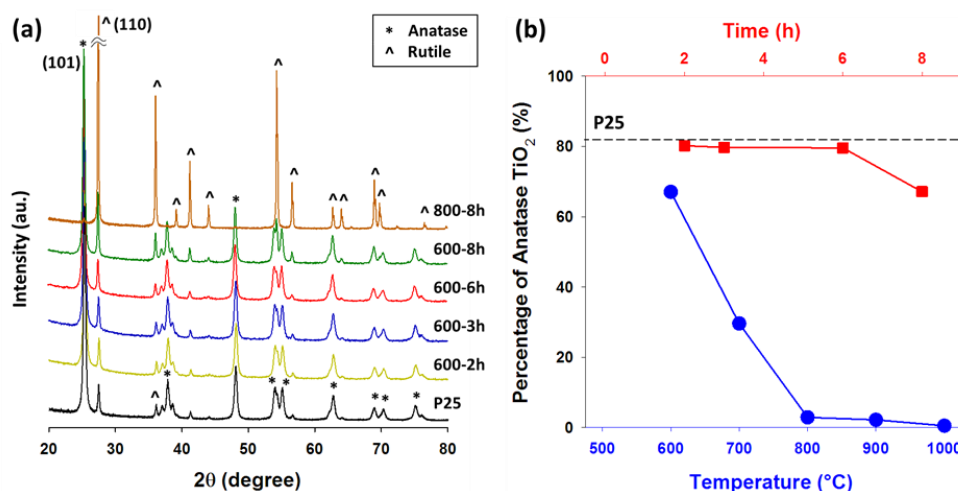

Figure 8. (a) XRD patterns of the composite hollow fibers and Degussa P25 titanium dioxide (as-received) over 20 – 80° 2θ region, and (b) the weight fraction of the anatase phase of TiO$_2$ a function of calcination temperature (blue circles) and time (red squares). Diffraction peak of the rutile phase (110) at 27.4° 2θ of the 800-8h sample is truncated for clarity in Fig. 8(a) and the black dotted line in Fig. 8(b) represents the weight fraction of anatase TiO$_2$ calculated for the P25 TiO$_2$.

Fig. 9 shows the percentage of photo-degradation of AO7 dye by the titania carbon hollow fibers membranes after 1 h of UV exposure with different calcination conditions. The data shown in Fig. 9 has been corrected for the 30 mins of dark sorption in each test and this was estimated to be between 4 and 7% in the cases of microporous hollow fiber samples [54]. In both series of data, there is a strong dependence of photocatalytic efficiency on calcination temperature and time. It can be observed that at both extremities of the temperature range, there is negligible AO7 degradation (< 2%) whilst the maximum region is found near 600–700 °C (43–41%), after which it decreases slowly. Similarly, the degradation profile of the time series shows a rapid surge from 0% (2 h) to 76% (3 h) and plateau to 90.4% at 6 h followed by a large drop to 43% at 8 h, despite all the samples contains very high proportion of the anatase TiO$_2$ phases. In both data series, it is observed that further increasing the calcination temperature or time would only result in a decrease in the degradation percentage of AO7 meaning a reduced photocatalytic activity of the composite hollow fibers. In contrast, insufficient temperature or time of calcination resulted in no degradation at all suggesting that the photoactivity of these composite hollow fibers is either non-active or hampered by the presence of a high concentration of amorphous carbon. Thus, this demonstrates that there is a compromise between calcination temperature and time. Although both the calcination temperature and time equally play important roles in controlling the photocatalytic properties of these composite hollow fibers, to gain shorter fabrication times, calcination temperature must be elevated, and vice versa.
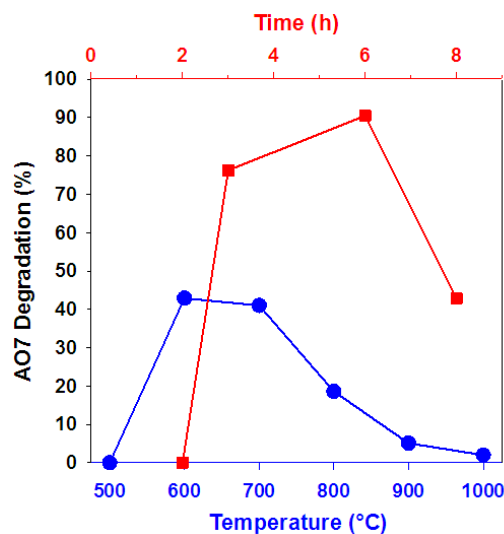
13

Figure 9. Percent degradation of AO7 by TiO$_2$ carbon composite hollow fibers after 1 h under UV irradiation as a function of calcination temperature (blue circles) and time (red squares) using 50 mg of hollow fiber and 20 ppm of AO7.

Overall, the properties and photocatalytic performance of the two series of hollow fibers indicates that there is a critical window of calcination temperature and time in this study. The hollow fibers prepared at 3 and 6 h at 600 °C calcination condition were selected for further membrane evaluation. These fibers were optimized to produce the carbon matrix with a good balance between porosity, chemical composition, mechanical strength and photocatalysis

3.3.2 Water Permeation

Fig. 10 shows the water flux of the 3 and 6 h hollow fiber membranes in deionized water and AO7 feed solutions in the dark and with UV irradiation in a customized dead-end filtration mode. During the membrane testing, both membranes continued to operate under pervaporation without any pore-wetting effect, which was however observed on the 8 h fiber during the first 30 sec and was excluded from further study. It was found that both membranes achieved greater than 99% rejection of AO7 in the permeate water demonstrating that these membranes are selectively permeable towards water molecules.
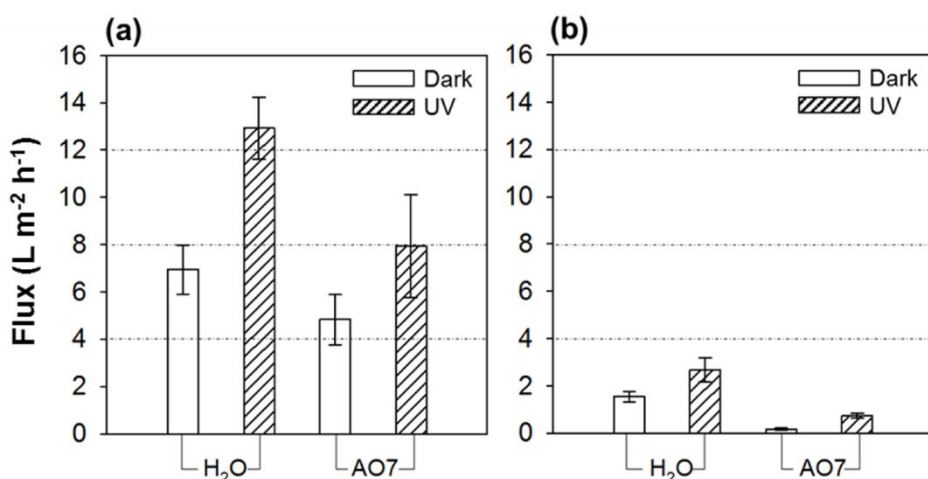
Figure 10. Pervaporation performance of TiO_2 carbon composite hollow fiber membranes prepared by the (a) 600-3h and (b) 600-6h of calcination time in deionized water and AO7 solutions (20 ppm) with/without UV irradiation using 4 cm of hollow fiber membrane length (surface area ~1.5×10^{-4} m^2). Data and error bar represent the mean ± two standard deviations (95% confidence interval) from three measurements.

Clearly in all of the testing conditions, the 3 h membranes out-performed the 6 h membranes because of the higher water flux values. In Fig. 10 (a), the 3 h membranes achieved the highest water fluxes of 6.9 (H_2O/dark), 12.9 (H_2O/UV) 4.8 (AO7/dark) and 7.9 L m^{-2} h^{-1} (AO7/UV), in comparison to 1.5 (H_2O/dark), 2.7 (H_2O/UV), 0.2 (AO7/dark) and 0.7 L m^{-2} h^{-1} (AO7/UV) for the 6 h membranes (Fig. 10(b)). In fact, the water fluxes produced by the 3 h membranes are very comparable to the water permeability of the TiO_2 hollow fiber (12.2 L m^{-2} h^{-1}) and the TiO_2/Al_2O_3 composite membranes (7.7 L m^{-2} h^{-1}) reported by Zhang *et al.*[30] and Choi *et al.*[16], respectively. Nevertheless, there are some interesting trends and patterns worthy of discussion, which is provided in the next section.

4. Discussions

The calcination process is routinely carried out to produce inorganic membranes with controlled porosity for a variety of separation applications. In this work, a low-temperature calcination protocol without the use of any specialized gases was chosen, which is unconventional for the normal thermal processing of carbon and titania hollow fibers described in the literature. It was found that the PEI polymer binder will form an amorphous carbon matrix by partially decomposition within this prescribed treatment protocol. This was proven by the SEM (Fig. 3), TGA (Fig. 5) and N_2 physisorption (Fig. 6) results as the final composite hollow fibers possess a high degree of microporosity in molecular dimensions typically reported for the carbon matrix. This property is directly responsible for the molecular-sieving properties of the membranes produced in this work. Another motivation for adopting this calcination protocol is optimizing the phase

15

concentration of anatase TiO_2 by keeping the calcination temperature threshold at 600 °C. Both chemical constituents that co-exist in two distinct phases within these hollow fibers are essential in producing the desired functionalities and properties for this study.

Fig. 11 displays the schematics of the hollow fiber formation during the calcination process. In Fig. 11(a), the dry green fiber consists of the PEI binder and the TiO_2 nanoparticles that are embedded within the polymer matrix. Upon calcination at low temperatures (600 °C) as shown in Fig. 11(b), the degree of pyrolysis and partial decomposition of PEI to carbonaceous char can be achieved, particularly in a temporal-controlled manner as evidenced by the characterization results of the time hollow fibers series. Also under this condition, the TiO_2 nanoparticles remain morphologically stable and un-sintered. Therefore, the microporous char forms between the voids of the TiO_2 nanoparticles imparting good mechanical strength. However, embedment of the TiO_2 nanoparticles by the carbon matrix led to a compromise in the photocatalytic efficiency because only the external surface of the fibers, where the anatase TiO_2 is accessible by the UV and AO7 molecules, can be considered photoactive. This is generally confined to a surface depth of a few hundreds of nanometer [15, 16].

In contrast, when the calcination temperature is raised above 700 °C, the char completely decomposes [55] and exposing the TiO_2 nanoparticles and the inter-particle voids. Furthermore, the titania nanoparticles are observed to undergo a phase transformation from the anatase phase to rutile and brokite phases [30]. During this process, some densification also takes place but the structural integrity of the hollow fibers becomes much weaker due to an increase concentration of surface defects and internal stress fractures. Hence, the mechanical strength diminishes with the loss of char. However, upon reaching close to 1000 °C, the TiO_2 nanoparticles start to be sintered together, which leads to an overall improved mechanical property which is in good agreement with these references [56, 57]. Despite the observable improvement, this process is marked by the loss of photoactivity due to the disappearance of preferred anatase phase of the TiO_2 nanoparticles.
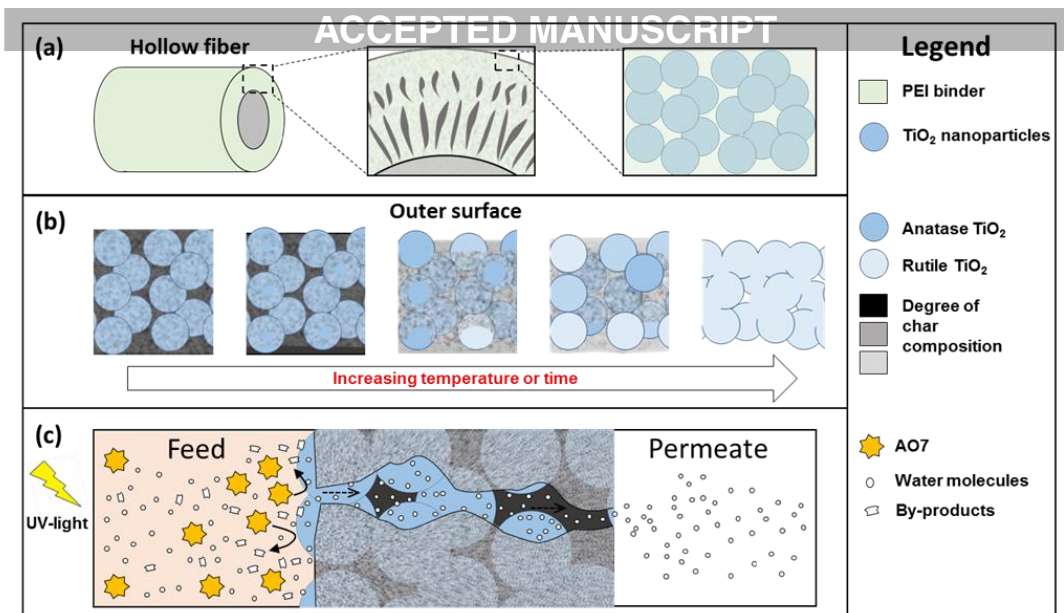
Figure 11. Schematic representation of the (a) green hollow fiber, (b) calcined composite hollow fibers with increasing calcination temperature or time, and (c) idealized pore structure of the composite matrix and diffusions of water molecules through a non-homogenous pore during photocatalysis-membrane operation.

Based on the results of the membrane performance, the hollow fibers were clearly capable of rejecting AO7 whilst producing purified water in the permeate stream. This implies that the composite hollow fibers were able to provide a selective barrier between the water and the dye molecules. In this work, the carbon matrix obviously plays the dominant role in imparting membrane selectivity due to its highly microporous texture as demonstrated by the N_2 physisorption results (Fig. 6). As shown in Fig. 11(c), the pore system of the carbon matrix is assumed to be non-homogeneous as it consists of a variation of size, shape and connectivity making up for both microporous constrictions and wider openings. It is generally accepted that the constrictions are responsible for selectivity, while the openings contribute to the majority of pore volume and thus are responsible for permeability. According to the transport mechanism of the carbon membranes [20], separation is caused by passage of smaller molecules through the pores while the larger molecules are obstructed. Such characteristic pore texture is consistent with the amorphous carbon membranes typically reported in the literature [20, 58]. Therefore, as shown in this study that the carbon matrix offers the fine-tuning of porosity and pore volume, which are extremely important for determining water flux of the hollow fibers for water production as membranes. This is exemplified by numerous studies of microporous ceramic membranes for desalination [59-61] and alcohol pervaporation [62-64]. On the other hand, highly mesoporous membranes, although lead to a high water production, will fail to separate the solute from water due to pore-wetting effect [39, 65].

In the context of this work, the constrictions in the carbon matrix have molecular dimensions between the size of the water (kinetic diameter = 2.6 Å) [66] and the much larger AO7 molecules

17

(9.4 Å), thereby working as a sieve. Note that the molecular size of AO7 molecule is estimated based on its chemical structure and is in good agreement with the calculation derived from the Stokes-Einstein equation [67, 68] using polyethylene glycol standards [69]. Although the N_2 physisorption results showed that the average pore diameters of the 3 and 6 h hollow fibers are recorded at 1.76 and 1.82 nm respectively, these results merely indicate the mean average of all the pore sizes (micropores and mesopores) that are measured by the N_2 gas. For even smaller constrictions that are less than the kinetic diameter of the N_2 gas (d_k = 3.65 Å), they simply exist outside of the detectable limit. Therefore, the N_2 physisorption technique is often used as qualitative comparison to assess the trend of pore size distribution and pore evolution. Nevertheless, both of these hollow fibers demonstrated the molecular-sieving property by producing clean permeate water with over 99% of the dye rejection during pervaporation, which is a true testament of the existence of micropore constrictions below 9.4 Å.

During the process of pervaporation, the hollow fibers not only provided the selectivity and water transport, but they also showed profound changes in response to the presence of AO7 molecules and UV irradiation. To further elucidate the effect of membrane fouling and photo-induction, Table 2 shows the calculated ratios of water flux with respect to feed condition (AO7/H₂O) with and without UV, and the exposure environment (UV/Dark) in only water or AO7 solution. The rationale of water flux ratios is depicted in Fig. 12 which shows a flowchart of testing conditions and correlations.

Table 2. Calculated ratios of water flux of the 600-3h and 600-6h hollow fibers with respect to feed conditions and exposure environments.

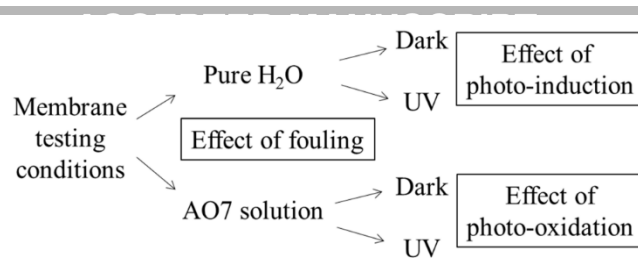|	Water Flux Ratios			
	AO7/H₂O		UV/Dark	
Membrane	Dark	UV	H₂O	AO7
600-3h	0.70	0.61	1.86	1.64
600-6h	0.11	0.27	1.74	4.11

Figure 12. Flow chart of membrane testing conditions and correlations.

As seen in Table 2 and Fig. 12, the presence of AO7 molecules in the feed under the dark shows that the total value of water flux could not be fully restored as reflected by the reduced $AO7/H_2O$ ratios of 0.70 (600-3h) and 0.11 (600-6h) for both membranes. In comparison, AO7 molecules significantly inhibited the water flux especially for the 6 h fiber. This indicates a greater extent of membrane fouling is experienced by the 6 h fiber during filtration. On the other hand, by comparing $AO7/H_2O$ water flux ratios in the presence of UV, the effect produced a 250% increase (0.27/0.11) in the water flux ratio for the 6 h fibers. The analysis demonstrates that there is a significant flux recovery upon application of the UV light, which suggests that AO7 fouling can be remediated as seen in the case of the 6 h membrane. In contrast, the initial fouling in the 3 h membrane was comparatively much less hence the flux recovery for the 3 h fiber was deemed insignificant. These differences in the behaviour can be explained by two membrane properties, namely porosity and hydrophilicity.

According to the textural results produced by N_2 physisorption (Fig. 6 and Table 1), the textural differences between the 3 and 6 h fibers lies in the increase of the total porosity, particularly due to the mesoporous domain. This change in porosity causes the relative micropore proportion to decrease as the calcination time doubles from 3 to 6 h. The enlargement of the total porosity seen in the 6 h fibers did not produce a higher water flux in comparison, but it actually caused a greater propensity of pore blocking by the AO7 molecules. As a result of this, the water flux (AO7/dark) only reached 11% of the pure water flux under the dark condition. Indeed, the presence of the AO7 molecules, with a 3.6 times larger than the size of a water molecule, will not only obstruct the membrane pores but will also hinder the water diffusion in the solution. The problem is also compounded by the fact that membrane pore blocking will lead to a reduction in transmembrane pressure, and thus results in an overall loss of permeate water production. In contrast, when UV is applied, the water recovery and defouling potential are observed to be very significant for the 6 h fibers because of a larger surface exposure of TiO_2 nanoparticles and a greater surface-to-AO7 contact from pore plugging. Hence, the flux ratio increased 2.5 times (0.27/0.11).

Another insight provided by the flux ratios in Table 2 is revealed by examining the effect of the exposure environment (UV/Dark) for a given feed condition (pure water or AO7 solution). Based the results, both fibers show a water flux enhancement when UV is used regardless of the feed condition. Under the pure water condition, the increase of water flux is 86% (3 h) and 74% (6 h) when UV is applied, which demonstrate that both hollow fibers become much more permeable. It is not surprising that the composite hollow fibers have such unique functionality under the

influence of UV light. This can be explained by the fact that TiO_2 nanoparticles are hydrophilic by nature and have been described to express the behaviour of photo-induced super-hydrophilicity [27, 36]. This photo-induction effect has been reported to cause an increase in the water transport through composite TiO_2 membranes [70, 71], which is also supported by the results in this study. Furthermore, the most profound enhancement is seen again in the 6 h membranes which produced the largest UV/Dark ratio of 4.11 in the AO7 feed. As shown by Fig. 11(c), when the membranes are irradiated by UV, the TiO_2 nanoparticles on the outer surface become super-hydrophilic, and at the same time become activated, causing the rapid decomposition of the AO7 molecules on the membrane surface. In turn, this resulted in both an increase in water affinity and a lesser degree of pore obstruction simultaneously, and thus, the water flux is enhanced 4-folds. In contrast, the 3 h membranes exhibited a lesser extent of AO7 fouling and lesser amount of exposed TiO_2 nanoparticles on the membrane surface, hence the photo-inductive effect (UV/Dark ratio of 1.64) is observed considerably smaller.

5. Conclusions

In this study, the syntheses of the composite hollow fibers were optimized for physicochemical, mechanical and photocatalytic properties by changing the calcination temperatures (500 to 1000 °C for 8 h) followed by times (2 to 8 h at 600 °C). It was found that by increasing the calcination temperature from 500 to 900 °C that the hollow fibers show a decreasing trend in bending modulus and photocatalysis. This was respectively due to the effect of thermal decomposition of the polymer binder and thermally-induced transformation of anatase to rutile phases of the titania nanoparticles. By limiting the calcination temperature to 600 °C, it was demonstrated that the hollow fiber membranes displayed multi-functional properties. The titania nanoparticles within these hollow fibers retained a high proportion of the anatase phase whilst the polymer binder was partially decomposed and pyrolyzed to form an amorphous, microporous carbon, which not only enhanced the surface area and pore volume, but also overcoming the trade-off between the bending modulus (~34 MPa) and photocatalytic degradation (> 90%) of AO7. The membrane performance of optimized photocatalytic hollow fibers (600-3h and 600-6h) were found to fully reject AO7 whilst producing purified water in the permeate stream via molecular-sieving process. The 600-3h membrane achieved the highest water fluxes of 6.9 (H_2O/dark), 12.9 (H_2O/UV) 4.8 (AO7/dark) and 7.9 L m^{-2} h^{-1} (AO7/UV), which are generally 5- to 10-folds larger than that of the 600-6h membrane. Notably, the effects of super-hydrophilicity and defouling potential of both membranes under the influence of UV light, especially for the 600-6h hollow fiber, are attributed to the photo-activation of the titania nanoparticles on the membrane surface. In summary, these hollow fibers demonstrate that they are excellent candidates for future studies regarding membrane scale-up and long-term performance stability in real environmental water matrices, and the potential to significantly reduce the processing and energy requirements for water treatment applications.

Acknowledgments

References

[1] D.S. Sholl, J.K. Johnson, Materials science: making high-flux membranes with carbon nanotubes, Science, 312 (2006) 1003-1004.

[2] R.M. de Vos, H. Verweij, High-selectivity, high-flux silica membranes for gas separation, Science, 279 (1998) 1710-1711.

[3] M.N. Chong, B. Jin, C.W.K. Chow, C. Saint, Recent developments in photocatalytic water treatment technology: A review, Water Res., 44 (2010) 2997-3027.

[4] C. Fernández, M.S. Larrechi, M.P. Callao, An analytical overview of processes for removing organic dyes from wastewater effluents, TrAC - Trends Anal. Chem., 29 (2010) 1202-1211.

[5] J. Mansouri, S. Harrisson, V. Chen, Strategies for controlling biofouling in membrane filtration systems: Challenges and opportunities, J. Mater. Chem., 20 (2010) 4567-4586.

[6] R. Andreozzi, V. Caprio, A. Insola, R. Marotta, Advanced oxidation processes (AOP) for water purification and recovery, Catal. Today, 53 (1999) 51-59.

[7] W.H. Glaze, J.W. Kang, D.H. Chapin, The chemistry of water treatment processes involving ozone, hydrogen peroxide and ultraviolet radiation, Ozone: Sci. Eng., 9 (1987) 335-352.

[8] J.J. Pignatello, E. Oliveros, A. MacKay, Advanced oxidation processes for organic contaminant destruction based on the fenton reaction and related chemistry, Crit. Rev. Environ. Sci. Technol., 36 (2006) 1-84.

[9] A. Markowska-Szczupak, K. Ulfig, A.W. Morawski, The application of titanium dioxide for deactivation of bioparticulates: An overview, Catal. Today, 169 (2011) 249-257.

[10] M.A. Lazar, S. Varghese, S.S. Nair, Photocatalytic water treatment by titanium dioxide: Recent updates, Catalysts, 2 (2012) 572-601.

[11] R. Molinari, L. Palmisano, E. Drioli, M. Schiavello, Studies on various reactor configurations for coupling photocatalysis and membrane processes in water purification, J. Membr. Sci., 206 (2002) 399-415.

[12] W. Xi, S.U. Geissen, Separation of titanium dioxide from photocatalytically treated water by cross-flow microfiltration, Water Res., 35 (2001) 1256-1262.

[13] X. Qu, P.J.J. Alvarez, Q. Li, Applications of nanotechnology in water and wastewater treatment, Water Res., 47 (2013) 3931-3946.

[14] H. Tong, S. Ouyang, Y. Bi, N. Umezawa, M. Oshikiri, J. Ye, Nano-photocatalytic materials: Possibilities and challenges, Adv. Mater., 24 (2012) 229-251.

[15] H. Choi, E. Stathatos, D.D. Dionysiou, Sol-gel preparation of mesoporous photocatalytic TiO_2 films and TiO_2/Al_2O_3 composite membranes for environmental applications, Appl. Catal. B: Environ, 63 (2006) 60-67.

[16] H. Choi, A.C. Sofranko, D.D. Dionysiou, Nanocrystalline TiO2 photocatalytic membranes with a hierarchical mesoporous multilayer structure: Synthesis, characterization, and multifunction, Adv. Funct. Mater., 16 (2006) 1067-1074.

[17] S. Leong, A. Razmjou, K. Wang, K. Hapgood, X. Zhang, H. Wang, TiO2 based photocatalytic membranes: A review, J. Membr. Sci., 472 (2014) 167-184.

[18] X. Zhang, D.K. Wang, J.C. Diniz Da Costa, Recent progresses on fabrication of photocatalytic membranes for water treatment, Catal. Today, 230 (2014) 47-54.

[19] S. Liu, K. Li, Preparation TiO2/Al2O3 composite hollow fibre membranes, J. Membr. Sci., 218 (2003) 269-277.

[20] A.F. Ismail, L.I.B. David, A review on the latest development of carbon membranes for gas separation, J. Membr. Sci., 193 (2001) 1-18.

[21] Z. Wu, R. Faiz, T. Li, B.F.K. Kingsbury, K. Li, A controlled sintering process for more permeable ceramic hollow fibre membranes, Journal of Membrane Science, 446 (2013) 286-293.

[22] K.I. Okamoto, S. Kawamura, M. Yoshino, H. Kita, Y. Hirayama, N. Tanihara, Y. Kusuki, Olefin/paraffin separation through carbonized membranes derived from an asymmetric polyimide hollow fiber membrane, Ind. Eng. Chem. Res., 38 (1999) 4424-4432.

[23] S. Husain, W.J. Koros, Mixed matrix hollow fiber membranes made with modified HSSZ-13 zeolite in polyetherimide polymer matrix for gas separation, J. Membr. Sci., 288 (2007) 195-207.

[24] X. Li, Y. Chen, X. Hu, Y. Zhang, L. Hu, Desalination of dye solution utilizing PVA/PVDF hollow fiber composite membrane modified with TiO2 nanoparticles, J. Membr. Sci., 471 (2014) 118-129.

[25] L.Y. Yu, Z.L. Xu, H.M. Shen, H. Yang, Preparation and characterization of PVDF-SiO2 composite hollow fiber UF membrane by sol-gel method, J. Membr. Sci., 337 (2009) 257-265.

[26] L.Y. Yu, H.M. Shen, Z.L. Xu, PVDF-TiO2 composite hollow fiber ultrafiltration membranes prepared by TiO2 sol-gel method and blending method, J. Appl. Polym. Sci., 113 (2009) 1763-1772.

[27] X. Chen, S.S. Mao, Titanium dioxide nanomaterials: Synthesis, properties, modifications and applications, Chem. Rev., 107 (2007) 2891-2959.

[28] D.A.H. Hanaor, C.C. Sorrell, Review of the anatase to rutile phase transformation, J. Mater. Sci., 46 (2011) 855-874.

[29] X. Zhang, T. Zhang, J. Ng, J.H. Pan, D.D. Sun, Transformation of bromine species in TiO2 photocatalytic system, Environ. Sci. Technol., 44 (2009) 439-444.

[30] X. Zhang, D.K. Wang, D.R.S. Lopez, J.C. Diniz da Costa, Fabrication of nanostructured TiO2 hollow fiber photocatalytic membrane and application for wastewater treatment, Chem. Eng. J., 236 (2014) 314-322.

[31] J.T. Dewolf, F.P. Beer, E.R. Johnston, Mechanics of Materials, McGraw-Hill Higher Education, New York, 2009.

[32] R. Rossmanith, C.K. Weiss, J. Geserick, N. Hüsing, U. Hörmann, U. Kaiser, K. Landfester, Porous anatase nanoparticles with high specific surface area prepared by miniemulsion technique, Chem. Mater., 20 (2008) 5768-5780.

[33] C.S. Kim, I.M. Kwon, B.K. Moon, J.H. Jeong, B.C. Choi, J.H. Kim, H. Choi, S.S. Yi, D.H. Yoo, K.S. Hong, J.H. Park, H.S. Lee, Synthesis and particle size effect on the phase transformation of nanocrystalline TiO2, Mater. Sci. Eng., 27 (2007) 1343-1346.

[34] X. Zhang, D.D. Sun, G. Li, Y. Wang, Investigation of the roles of active oxygen species in photodegradation of azo dye AO7 in TiO2 photocatalysis illuminated by microwave electrodeless lamp, J. Photochem. Photobiol., A, 199 (2008) 311-315.

[35] X. Zhang, Y. Wang, G. Li, Effect of operating parameters on microwave assisted photocatalytic degradation of azo dye X-3B with grain TiO2 catalyst, J. Mol. Catal. A: Chem., 237 (2005) 199-205.

[36] O. Carp, C.L. Huisman, A. Reller, Photoinduced reactivity of titanium dioxide, Prog. Solid State Chem., 32 (2004) 33-177.

[37] M.A. Fox, M.T. Dulay, Heterogeneous photocatalysis, Chem. Rev., 93 (1993) 341-357.

[38] X. Zhang, A.J. Du, P. Lee, D.D. Sun, J.O. Leckie, TiO2 nanowire membrane for concurrent filtration and photocatalytic oxidation of humic acid in water, J. Membr. Sci., 313 (2008) 44-51.

[39] M. Elma, D.K. Wang, C. Yacou, J.C. Diniz da Costa, Interlayer-free P123 carbonised template silica membranes for desalination with reduced salt concentration polarisation, J. Membr. Sci., 475 (2015) 376-383.

[40] B.F.K. Kingsbury, K. Li, A morphological study of ceramic hollow fibre membranes, J. Membr. Sci., 328 (2009) 134-140.

[41] B.F.K. Kingsbury, Z. Wu, K. Li, A morphological study of ceramic hollow fibre membranes: A perspective on multifunctional catalytic membrane reactors, Catal. Today, 156 (2010) 306-315.

[42] D.R. Schmeda-Lopez, S. Smart, E.H.M. Nunes, D. Vasconcelos, W.L. Vasconcelos, M. Bram, W.A. Meulenberg, J.C. Diniz Da Costa, Stainless steel hollow fibres - Sintering, morphology and mechanical properties, Sep. Purif. Technol., 147 (2015) 379-387.

[43] D.K. Wang, M. Elma, J. Motuzas, W.C. Hou, D.R. Schmeda-Lopez, T. Zhang, X. Zhang, Physicochemical and Photocatalytic Properties of Carbonaceous Char and Titania Composite Hollow Fibers for Wastewater Treatment, Carbon, 109 (2016) 182-191.

[44] X. Zhang, J.H. Pan, A.J. Du, J. Ng, D.D. Sun, J.O. Leckie, Fabrication and photocatalytic activity of porous TiO2 nanowire microspheres by surfactant-mediated spray drying process, Mater. Res. Bull., 44 (2009) 1070-1076.

[45] X. Tan, S. Liu, K. Li, Preparation and characterization of inorganic hollow fiber membranes, J. Membr. Sci., 188 (2001) 87-95.

[46] P. Haworth, S. Smart, J. Glasscock, J.C. Diniz da Costa, High performance yttrium-doped BSCF hollow fibre membranes, Sep. Purif. Technol., 94 (2012) 16-22.

[47] A. Leo, S. Smart, S. Liu, J.C. Diniz da Costa, High performance perovskite hollow fibres for oxygen separation, Journal of Membrane Science, 368 (2011) 64-68.

[48] S. Liu, K. Li, R. Hughes, Preparation of porous aluminium oxide (Al2O3) hollow fibre membranes by a combined phase-inversion and sintering method, Ceram. Int., 29 (2003) 875-881.

[49] S. Liu, X. Tan, K. Li, R. Hughes, Preparation and characterisation of SrCe0.95Yb0.05O2.975 hollow fibre membranes, J. Membr. Sci., 193 (2001) 249-260.

[50] A.A. Gribb, J.F. Banfield, Particle size effects on transformation kinetics and phase stability in nanocrystalline TiO2, Am. Mineral., 82 (1997) 717-728.

[51] J.P. Jolivet, Metal Oxide Chemistry and Synthesis From Solution to Solid State, Wiley, Chichester, 2000.

[52] K. Yanagisawa, J. Ovenstone, Crystallization of anatase from amorphous titania using the hydrothermal technique: Effects of starting material and temperature, J. Phys. Chem. B, 103 (1999) 7781-7787.

[53] E. Kordouli, V. Dracopoulos, T. Vaimakis, K. Bourikas, A. Lycourghiotis, C. Kordulis, Comparative study of phase transition and textural changes upon calcination of two commercial titania samples: A pure anatase and a mixed anatase-rutile, J. Solid State Chem., 232 (2015) 42-49.

[54] E. Kordouli, K. Bourikas, A. Lycourghiotis, C. Kordulis, The mechanism of azo-dyes adsorption on the titanium dioxide surface and their photocatalytic degradation over samples with various anatase/rutile ratios, Catal. Today, 252 (2015) 128-135.

[55] W.N.W. Salleh, A.F. Ismail, Effect of Stabilization Condition on PEI/PVP-Based Carbon Hollow Fiber Membranes Properties, Sep. Sci. Technol., 48 (2013) 1030-1039.

[56] J.G. Yu, H.G. Yu, B. Cheng, X.J. Zhao, J.C. Yu, W.K. Ho, The Effect of Calcination Temperature on the Surface Microstructure and Photocatalytic Activity of TiO2 Thin Films Prepared by Liquid Phase Deposition, J. Phys. Chem. B, 107 (2003) 13871-13879.

[57] J. Yu, H. Yu, B. Cheng, C. Trapalis, Effects of calcination temperature on the microstructures and photocatalytic activity of titanate nanotubes, J. Mol. Catal. A: Chem., 249 (2006) 135-142.

[58] S.M. Saufi, A.F. Ismail, Fabrication of carbon membranes for gas separation - A review, Carbon, 42 (2004) 241-259.

[59] C.X.C. Lin, L.P. Ding, S. Smart, J.C. Diniz da Costa, Cobalt oxide silica membranes for desalination, J. Colloid Interface Sci., 368 (2012) 70-76.

[60] B.P. Ladewig, Y.H. Tan, C.X.C. Lin, K. Ladewig, J.C. Diniz da Costa, S. Smart, Preparation, Characterization and Performance of Templated Silica Membranes in Non-Osmotic Desalination, Materials, 4 (2011) 845-856.

[61] S. Wijaya, M.C. Duke, J.C. Diniz da Costa, Carbonised template silica membranes for desalination, Desalination, 236 (2009) 291-298.

[62] J. Wang, M. Kanezashi, T. Yoshioka, T. Tsuru, Effect of calcination temperature on the PV dehydration performance of alcohol aqueous solutions through BTESE-derived silica membranes, J. Membr. Sci., 415–416 (2012) 810-815.

[63] J. Wang, T. Tsuru, Cobalt-doped silica membranes for pervaporation dehydration of ethanol/water solutions, J. Membr. Sci., 369 (2011) 13-19.

[64] H.L. Castricum, G.G. Paradis, M.C. Mittelmeijer-Hazeleger, R. Kreiter, J.F. Vente, J.E. Ten Elshof, Tailoring the separation behavior of hybrid organosilica membranes by adjusting the structure of the organic bridging group, Adv. Funct. Mater., 21 (2011) 2319-2329.

[65] M. Elma, C. Yacou, J.C. Diniz da Costa, D.K. Wang, Performance and long term stability of mesoporous silica membranes for desalination, Membranes, 3 (2013) 136-150.

[66] J. Lin, S. Murad, A computer simulation study of the separation of aqueous solutions using thin zeolite membranes, Mol. Phys., 99 (2001) 1175-1181.

[67] J.T. Edward, Molecular volumes and the Stokes-Einstein equation, J. Chem. Educ., 47 (1970) 261-270.

[68] H.P. Erickson, Size and shape of protein molecules at the nanometer level determined by sedimentation, gel filtration, and electron microscopy, Biol. Proced. Online, 11 (2009) 32-51.

[69] V. Smentkowski, Diffusion Ordered Spectroscopy and Materials, in GE Global Research, http://www.geglobalresearch.com/blog/diffusion-ordered-spectroscopy-and-materials, 25/07/2012, accessed on 14/08/2016.

[70] N.G. Moustakas, F.K. Katsaros, A.G. Kontos, G.E. Romanos, D.D. Dionysiou, P. Falaras, Visible light active TiO2 photocatalytic filtration membranes with improved permeability and low energy consumption, Catal. Today, 224 (2014) 56-69.

[71] J. Yu, M. Zhou, H. Yu, Q. Zhang, Y. Yu, Enhanced photoinduced super-hydrophilicity of the sol–gel-derived TiO2 thin films by Fe-doping, Mater. Chem. Phys., 95 (2006) 193-196.

Highlights

- Single-step low temperature pyrolysis offers robust inorganic composite hollow fibers
- Hollow fiber with carbon molecular sieve and photocatalytic titania nanoparticles
- Enhanced bending stress of 34 MPa and 90.4% acid orange dye photo-degradation
- Maximum water flux of 7.9 L m^{-2} h^{-1} and over 99% dye rejection
- Fibers exhibit super-hydrophilicity and defouling potential under UV irradiation